

A hybrid boundary element method for shallow water acoustic propagation over an irregular bottom

Stéphan Grilli*, Torstein Pedersen & Peter Stepanishen

Ocean Engineering Department, University of Rhode Island, Narragansett, RI 02882, USA

A hybrid numerical model combining a boundary element method (BEM) and eigenfunction expansions is developed to solve acoustic wave propagation in shallow water. Waves are assumed harmonic and, therefore, the governing equation reduces to a Helmholtz equation.

Accurate numerical integration techniques are implemented in the BEM, for calculating singular and quasi-singular integrals. For the latter, an adaptive integration technique is developed and tested for computational domains with very small aspect ratios, representative of shallow water environments.

The model is validated by comparing the numerical solution to analytic solutions for problems with simple boundary geometries (e.g. rectangular, step, and sloped domains). Results indicate good agreement between the two solutions. Effects of node resolution, adaptive integrations, and number of modes in radiated fields, on the accuracy of the solution, are assessed.

Finally, the model is used to study acoustic transmission over a rectangular bump in the bottom, as a function of frequency and bump geometry. Expected results are obtained below the first cut-off frequency over the bump, i.e. the transmission of energy beyond the bump through evanescent modes. A similar effect is commonly noted in layered media and is known as 'tunneling'. © 1998 Elsevier Science Ltd. All rights reserved

Key words: Underwater acoustic, shallow water acoustic, wave propagation, boundary element method, hybrid-BEM.

1 INTRODUCTION

The study of ocean acoustic wave propagation has traditionally been directed to deep water environments. Recently, however, due to increasing concern for coastal areas, studies have been focusing more and more on shallow water environments. In the US Navy, for instance, the support of littoral warfare units has been placing increasing emphasis of research and development in underwater acoustics, within the shallower water regions. Urlick¹ defines shallow water acoustic propagation as the 'propagation to distances at least several times the water depth, under conditions where both the surface and bottom boundaries have an effect on transmission'.

The present study focuses on the numerical modeling of shallow water acoustic propagation, in the frequency domain, over irregular (rigid) bottom topography. Numer-

ous techniques have been used in the past to model acoustic wave propagation. As indicated by Jensen et al.,² most of these methods can be classified as follows.

1. *Ray methods.* These methods are most commonly used in deep water. They assume an asymptotic form of the homogeneous wave equation and are thus restricted to high frequencies. Additionally, such methods deal with bottom interactions only in an approximate manner; therefore they are not suitable in shallow water.
2. *Normal mode methods.* These methods are used for shallow water propagation in horizontally stratified media. They are best suited for low frequency problems but experience difficulties with domains which are both range and depth dependent.
3. *Parabolic equation methods.* These methods, despite their acceptable results for most range and depth dependent problems, are restricted to a small angle

*Corresponding author

approximation and, hence, experience difficulties for long range problems. Additionally, such methods neglect backscattering effects, which are likely to be important in very shallow water and near the shoreline.

As a result of the limitations of these commonly used methods, in the present study it is proposed to develop a numerical model applicable to range dependent shallow water acoustic propagation problems.

In the problems considered here, we assume a two-dimensional geometry; this is often representative of coastal regions which have little variation in the long shore direction. The solution of the wave equation, i.e. the acoustic pressure or the velocity potential, will be harmonic in time and, therefore, the governing equation will reduce to a Helmholtz equation. This equation can be transformed into a boundary integral equation (BIE) and accurately and efficiently solved using a higher-order boundary element method (BEM), together with relevant boundary conditions on the free surface and bottom boundaries (Γ_f and Γ_b in Fig. 1). In the present applications, lateral open boundaries are treated as radiation boundaries beyond which a constant depth region is assumed (Γ_{r1} and Γ_{r2} in Fig. 1). In such regions, radiated fields are represented by eigenfunction expansions, which provide relationships between the potential and its normal gradient along the radiation boundaries. These expansions are constructed using both propagating (i.e. real) and non-propagating (i.e. imaginary) acoustic modes. (A mode is propagating if its cut-off frequency is less than the frequency of excitation of the acoustic source(s). Non-propagating modes are commonly referred to as evanescent modes, since they decay exponentially with distance.) Due to the combination of analytical and BEM techniques, the present model is referred to as a hybrid boundary element model (HBEM). Note that shallow water geometries, typically, have large length to depth ratios, which can potentially lead to inaccuracies of the numerical integrations in the BEM. The *adaptive integration* technique developed by Grilli and Svendsen³ for the Laplace equation was modified and implemented to improve accuracy of integrations in these cases.

Two types of problems will be considered: (i) those with two open radiation boundaries, Γ_{r1} and Γ_{r2} (Fig. 1(a)), representing vertical ocean sections, typically containing bottom discontinuities (i.e. 'bumps'); (ii) those with one open radiation boundary, Γ_{r1} (Fig. 1(b)), representing vertical ocean sections intersecting the shoreline (i.e. 'wedges'). In all cases, a computational domain Ω , with arbitrary bottom geometry, is defined and the potential ϕ is discretized and numerically calculated on the model boundary Γ , under the excitation by (line) sources, S_i . Receivers, R_i , may be located in the domain, at which the acoustic response can be calculated as a function of the boundary solution.

The model developed will first be validated through solving problems with simple boundary geometries and comparing numerical results to analytical solutions, i.e. a

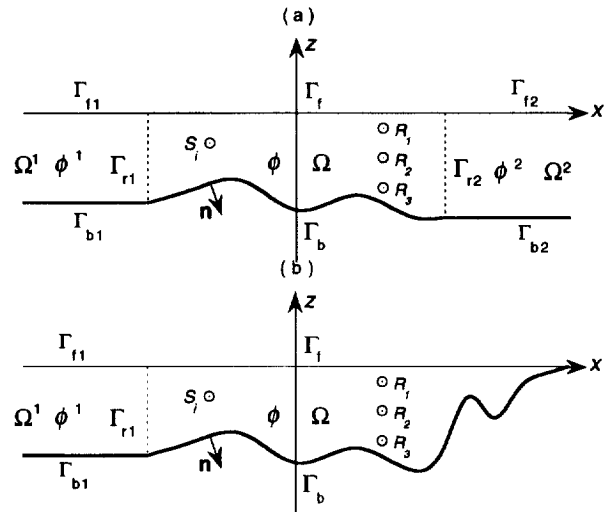


Fig. 1. Typical domain geometries in the HBEM model, for shallow water acoustic propagation problems in a vertical: (a) ocean section with bottom discontinuity ('bump'); (b) ocean section intersecting the shoreline ('wedge').

rectangular geometry, a bottom step, and a plane slope. These geometries are representative of shallow water and coastal bottom topographies. Finally, the validated model will be used to study problems for which the geometry prevents or complicates an analytic approach. Here, the transmission of acoustic energy over rectangular obstacles on the bottom, through a manner similar to the 'tunneling' phenomenon,² is investigated. This property is common to layered media where some layers can only accommodate evanescent modes; if the thickness of a layer is small, however, then the next layer of lesser impedance can be excited by exponentially decaying evanescent modes. The geometry in Fig. 1(a) is similar to such a layered media where, at lower frequencies, the shallower region Ω may have purely evanescent modes and the deeper regions Ω^1 and Ω^2 have propagating modes, like the layers on either side of the smaller layer that leaks energy.

2 THE MATHEMATICAL AND NUMERICAL MODEL

2.1 Governing equation

For *homogeneous harmonic* two-dimensional problems in the vertical plane, (x, z) , with constant sound velocity c , and assuming *ideal fluid theory*, the complex velocity potential can be defined as, $\Phi(x, z, t) = \phi(x, z) \exp(-j\omega t)$, with the velocity $\mathbf{u} = \nabla\Phi$, ω the acoustic wave circular frequency, and ϕ the complex potential amplitude (complex notations will be used throughout this text, with $j = \sqrt{-1}$).

In this case, the governing wave equation reduces to a Helmholtz equation for ϕ in domain Ω ,

$$\nabla^2\phi + k^2\phi = - \sum_{i=1}^{N_s} S_i \delta(x_{s_i}, z_{s_i}) \text{ in } \Omega \quad (1)$$

in which, $k = \omega/c$ is the wavenumber and S_i values denote (potential) strengths of N_s point sources at locations (x_{s_i}, z_{s_i}) (Fig. 1).

Using the free space Green's function, $G(r, r_l) = (j/4)H_0^{(1)}(kr)$, and its normal derivative, $\partial G(r, r_l)/\partial n = -k(j/4)H_1^{(1)}(kr)(\partial r/\partial n)$, both expressed in terms of Hankel functions, according to Green's second identify, eqn (1) transforms into the following boundary integral equation (BIE)

$$\alpha(\mathbf{r}_l)\phi(\mathbf{r}_l) + \int_{\Gamma(\mathbf{r})} \left\{ \frac{\partial G(\mathbf{r}, \mathbf{r}_l)}{\partial n} \phi(\mathbf{r}) - \frac{\partial \phi}{\partial n}(\mathbf{r})G(\mathbf{r}, \mathbf{r}_l) \right\} d\Gamma(\mathbf{r}) = \sum_{i=1}^{N_s} S_i G(\mathbf{r}_{s_i}, \mathbf{r}_l) = P_l \quad (2)$$

where \mathbf{r} and \mathbf{r}_l are position vectors for points on boundary Γ , $r = |\mathbf{r} - \mathbf{r}_l|$, \mathbf{n} is the outward normal vector, $\alpha(\mathbf{r}_l)$ is a geometric coefficient (equal to 1/2 on a smooth boundary and 1 inside the domain), and P_l denotes the source excitation vector.

2.2 Boundary conditions

Reference boundary geometries for two typical problems are indicated in Fig. 1.

2.2.1 Bottom and free surface conditions

The bottom is rigid, both inside the computational domain Ω and in radiation regions Ω^1 and Ω^2 . Hence, a no-flow condition applies,

$$\overline{\frac{\partial \phi}{\partial n}} = 0 \text{ on } \Gamma_b \text{ and } \Gamma_{b_i} \text{ (} i = 1, 2 \text{)} \quad (3)$$

where the overbar indicates a specified value.

At the steady free surface, in all regions, assuming atmospheric pressure $p = 0$, we obtain from the linearized Bernoulli equation,

$$p = -\rho_o \frac{\partial \Phi}{\partial t} = j\omega\rho_o\Phi = 0 \quad (4)$$

with ρ_o the fluid density, i.e. with no wave present,

$$\bar{\phi} = 0 \text{ on } \Gamma_f \text{ and } \Gamma_{f_i} \text{ (} i = 1, 2 \text{)} \quad (5)$$

2.2.2 Radiation condition

On open boundaries, Γ_{ri} ($i = 1, 2$), a radiation condition is specified such that the potential and its normal gradient are continuous from inside the computational domain to outside,

$$\phi^i = \phi \text{ and } \frac{\partial \phi^i}{\partial n} = \frac{\partial \phi}{\partial n} \text{ on } \Gamma_{ri} \text{ (} i = 1, 2 \text{)} \quad (6)$$

Assuming constant depth h^i in the exterior regions Ω^i , the potential on the open boundaries can be exactly represented by the following eigenfunction expansion, which satisfies the governing equation and both bottom and free surface

boundary conditions (eqns (3) and (5))⁴

$$\phi^i(x, z) = \sum_{m=1}^{\infty} A_m^i \sin(k_m^i z) e^{j\sqrt{k^2 - k_m^{i2}|x|}} \quad (7)$$

with the separation constant, $k_m^i = \pi(2m-1)/2h^i$, for the m th mode. From eqn (7), the potential normal gradient on the open boundaries reads,

$$\frac{\partial \phi^i}{\partial n} = j \sum_{m=1}^{\infty} A_m^i \sqrt{k^2 - k_m^{i2}} \sin(k_m^i z) e^{j\sqrt{k^2 - k_m^{i2}|x|}} \quad (8)$$

In order to derive an expression relating the potential and its gradient, we use the orthogonality property of the eigenfunctions,

$$\int_{-h^i}^0 \sin(k_l^i z) \sin(k_m^i z) dz = \frac{h^i}{2} \delta_{lm} \quad (9)$$

Hence, if we multiply the potential in eqn (7) by $\sin(k_l^i z)$ and integrate over depth, we obtain the expansion coefficients as,

$$A_l^i = \frac{2}{h^i} e^{-j\sqrt{k^2 - k_l^{i2}|x|}} \int_{-h^i}^0 \phi^i \sin(k_l^i z) dz \quad (10)$$

Substituting this result, for $l = m$, into eqn (8), truncating the expansion to N_m terms and using eqn (6), we obtain the sought after relationship between the potential and its normal gradient along the radiation boundaries,

$$\frac{\partial \phi}{\partial n} = \frac{2j}{h^i} \sum_{m=1}^{N_m} \sqrt{k^2 - k_m^{i2}} \sin(k_m^i z) \int_{-h^i}^0 \phi^i \sin(k_m^i z) dz \text{ on } \Gamma_{ri} \text{ (} i = 1, 2 \text{)} \quad (11)$$

which can be formally written as

$$\overline{\frac{\partial \phi}{\partial n}} = \mathcal{F}^i(\phi) \text{ on } \Gamma_{ri} \text{ (} i = 1, 2 \text{)} \quad (12)$$

The number of modes N_m required to accurately represent the solution in the exterior radiation regions will be discussed in a subsequent section on model validation.

2.3 Boundary integral equation

After substitution of the boundary conditions of eqns (3), (5) and (12) into eqn (2), the resulting BIE is given as

$$\alpha(\mathbf{r}_l)\phi(\mathbf{r}_l) - \int_{\Gamma_r} \frac{\partial \phi}{\partial n}(\mathbf{r})G(\mathbf{r}, \mathbf{r}_l) d\Gamma(\mathbf{r}) + \int_{\Gamma_b} \frac{\partial G(\mathbf{r}, \mathbf{r}_l)}{\partial n} \phi(\mathbf{r}) d\Gamma(\mathbf{r}) + \sum_{i=1}^{N_r} \int_{\Gamma_{ri}} \left\{ \frac{\partial G(\mathbf{r}, \mathbf{r}_l)}{\partial n} \phi(\mathbf{r}) + (-1)^i \mathcal{F}^i(\phi(\mathbf{r}))G(\mathbf{r}, \mathbf{r}_l) \right\} d\Gamma(\mathbf{r}) = P_l \quad (13)$$

where N_r denotes the number of radiation boundaries (1 or 2) in the problem, and the \pm signs are due to the orientation of boundaries Γ_{ri} .

2.4 Boundary discretization and discretized BIE

The BIE eqn (13) is solved using a boundary element method (BEM)⁵ in which the potential or its normal gradient (whichever is unknown) are calculated on the boundary by discretizing the BIE at N_n collocation nodes and numerically calculating the integrals. To do so, the boundary is divided into N_e small elements over which both the field variables and the geometry are approximated by polynomial shape functions (isoparametric elements). The integrals are evaluated, for each collocation node l , by summing contributions from elements over the boundary. The integration for element e begins by mapping the element onto a reference element of intrinsic coordinate $\xi \in [-1, +1]$, using the Jacobian, $\partial s^e / \partial \xi = \{(\partial x^e / \partial \xi)^2 + (\partial z^e / \partial \xi)^2\}^{1/2}$, and then interpolating the field variables and the geometry using the element nodal values and the shape functions, $N_j^d(\xi)$, which are analytically defined as polynomials of degree d in ξ , for a $(d + 1)$ -node reference element.

Introducing this discretization into eqn (2), an algebraic system of equations is obtained for $l = 1, \dots, N_n$ which, after introducing the boundary conditions as in eqn (13), is solved to provide the unknown field values at the collocation nodes along the boundary. Main integrals in the BIE can formally be divided into Dirichlet and Neuman integrals, defined as

$$\begin{aligned} & \int_{\Gamma} \frac{\partial \phi}{\partial n}(\mathbf{r}) G(\mathbf{r}, \mathbf{r}_l) d\Gamma(\mathbf{r}) \\ &= \sum_{n=1}^{N_n} \left\{ \sum_{e=1}^{N_e} \int_{-1}^{+1} N_{j(n)}^d(\xi) G(\mathbf{r}(\xi), \mathbf{r}_l) \frac{\partial s^e}{\partial \xi}(\xi) d\xi \right\} \frac{\partial \phi}{\partial n}(\mathbf{r}_{j(n)}) \\ &= \sum_{j=1}^{N_n} \left\{ \sum_{e=1}^{N_e} I_{d_l}^e \right\} \frac{\partial \phi_j}{\partial n} = \sum_{j=1}^{N_n} K_{d_l} \frac{\partial \phi_j}{\partial n} \end{aligned} \quad (14)$$

and

$$\begin{aligned} & \int_{\Gamma} \phi(\mathbf{r}) \frac{\partial G(\mathbf{r}, \mathbf{r}_l)}{\partial n} d\Gamma(\mathbf{r}) \\ &= \sum_{n=1}^{N_n} \left\{ \sum_{e=1}^{N_e} \int_{-1}^{+1} N_{j(n)}^d(\xi) \frac{\partial G(\mathbf{r}(\xi), \mathbf{r}_l)}{\partial n} \frac{\partial s^e}{\partial \xi}(\xi) d\xi \right\} \phi(\mathbf{r}_{j(n)}) \\ &= \sum_{j=1}^{N_n} \left\{ \sum_{e=1}^{N_e} I_{n_l}^e \right\} \phi_j = \sum_{j=1}^{N_n} K_{n_l} \phi_j \end{aligned} \quad (15)$$

respectively, where the index j denotes 'assembled' local nodal values for element e , expressed in the global node numbering n ; the Dirichlet and Neuman integrals for the e th element are indicated by $I_{d_l}^e$ and $I_{n_l}^e$ respectively.

In addition, as indicated in eqn (13), over the radiation boundaries, radiation integrals are calculated as ($i = 1, \dots, N_r$),

$$\begin{aligned} & \int_{\Gamma_{r_i}} \mathcal{F}^i(\phi(\mathbf{r})) G(\mathbf{r}, \mathbf{r}_l) d\Gamma(\mathbf{r}) \\ &= \sum_{j=1}^{N_{r_i}} \left\{ \sum_{m=1}^{N_m} \frac{2j}{h^i} \sqrt{k^2 - k_m^2} \int_{\Gamma_{r_i}} G(\mathbf{r}, \mathbf{r}_l) \sin(k_m^i z(\mathbf{r})) d\Gamma(\mathbf{r}) \right. \\ & \quad \left. \times \int_{\Gamma_{r_i}} N_j^d(\mathbf{r}) \sin(k_m^i z(\mathbf{r})) d\Gamma(\mathbf{r}) \right\} \phi(\mathbf{r}_j) \\ &= \sum_{j=1}^{N_{r_i}} \left\{ \sum_{m=1}^{N_m} K_{r_{l,m}}^i K_{r_{2,m}}^i \right\} \phi(\mathbf{r}_j) = \sum_{j=1}^{N_{r_i}} K_{r_{ij}}^i \phi(\mathbf{r}_j) \end{aligned} \quad (16)$$

where N_{r_i} denotes the number of discretization nodes on boundary Γ_{r_i} . The computation of integrals in eqn (16) is performed through a summation of contributions of elements on the radiation boundaries, after transformation to the reference element as indicated above.

Using eqns (14)–(16), the discretized system of equations corresponding to eqn (13) is obtained as

$$\begin{aligned} \alpha_l \phi_l - \sum_{f=1}^{N_f} K_{d_{lf}} \frac{\partial \phi_f}{\partial n} + \sum_{b=1}^{N_b} K_{n_{lb}} \phi_b \\ + \sum_{i=1}^{N_r} \sum_{r_j=1}^{N_{r_i}} \{K_{n_{r_i}} + (-1)^i K_{r_{r_i}}^i\} \phi_{r_j} = P_l \\ l = 1, \dots, N_n \end{aligned} \quad (17)$$

where, N_f and N_b denote the number of discretization nodes on boundary Γ_f and Γ_b , respectively, and the unknown potentials and potential normal gradients have been placed on the left-hand-side of the system.

The total number of complex unknowns in the linear system (eqn (17)) is $N_n = N_f + N_b + \sum_{i=1}^{N_r} N_{r_i}$, and coefficients in the system matrix are complex. Therefore, before solution, the system of equations is transformed into a real system which is double in size [$2N_n \times 2N_n$]. The final system of equations is solved using Khaletski's⁶ direct elimination method.

Finally, note that coefficients α_l in the discretized algebraic system (eqn (17)) are calculated using the *rigid mode method*.⁵

2.5 Regular and singular integrations

In eqns (14)–(16), the integrals are non-singular when the element node j is not equal to the collocation node l , ($j \neq l$). Gauss quadrature is used to evaluate such integrals over each element e .

When the collocation node is identical to an element node ($j = l$), the Green's function in the Dirichlet integrals and in radiation integrals $K_{r_l}^i$ becomes logarithmically singular as r approaches zero, as the limit of the Hankel function in the Green's function reads⁷

$$\lim_{kr(\xi) \rightarrow 0} H_0^{(1)}(kr(\xi)) = \left(1 + \frac{2j}{\pi} \gamma\right) + \frac{2j}{\pi} \ln\left(\frac{kr(\xi)}{2}\right) \quad (18)$$

where $\gamma = 0.5772\dots$ is Euler's constant.

Applying the kernel transformation method by Grilli et al.,⁸ these integrals will be expressed as a non-singular part, which will be evaluated using Gauss integration, and a singular part which will be evaluated using Berthod–Zabrowsky's method.⁹

More specifically, recalling expression (14) of the Dirichlet integrals for the e th element and using eqn (18), we obtain

$$I_{d_{ij}}^e = \frac{j}{4} \int_{-1}^{+1} f_j^e(\xi) \left\{ H_0^{(1)}(kr(\xi)) - \frac{2j}{\pi} \ln\left(\frac{kr(\xi)}{2}\right) \right\} d\xi \\ + \frac{j}{4} \int_{-1}^{+1} f_j^e(\xi) \left\{ \frac{2j}{\pi} \ln\left(\frac{kr(\xi)}{2}\right) \right\} d\xi \quad (19)$$

where $f_j^e(\xi) = N_j^d(\xi)(\partial s^e(\xi)/\partial \xi)$. If the logarithmic functions in eqn (19) are further expanded, we obtain

$$I_{d_{ij}}^e = \frac{j}{4} \int_{-1}^{+1} f_j^e(\xi) \left\{ H_0^{(1)}(kr(\xi)) - \frac{2j}{\pi} \ln\left(\frac{kr(\xi)}{2}\right) \right\} \\ + \frac{2j}{\pi} \ln\left(\frac{k}{2}\right) \int_{-1}^{+1} f_j^e(\xi) d\xi - \frac{1}{2\pi} \int_{-1}^{+1} f_j^e(\xi) \ln(r(\xi)) d\xi \quad (20)$$

According to eqn (18), the first integral in eqn (20) is regular. The second integral is identical to the Dirichlet integral for potential flow theory; hence, the kernel transformation technique by Grilli *et al.*⁸ can be used and we obtain the final form of the Dirichlet integral for the e th element as

$$I_{d_{ij}}^e = \int_{-1}^{+1} \left\{ f_j^e(\xi) \left\{ \frac{j}{4} H_0^{(1)}(kr(\xi)) + \frac{1}{2\pi} \ln\left(\frac{|\xi - \xi_l|}{2}\right) \right\} \right. \\ \left. - \frac{1}{2\pi} \left\{ f_j^e(\xi_{p1}\xi - \xi_{p2}) \xi_{p1} \ln \xi_{p1} \right. \right. \\ \left. \left. + f_j^e(\xi_{p2}\xi + \xi_{p1}) \xi_{p2} \ln \xi_{p2} \right\} \right\} d\xi \\ - \frac{1}{\pi} \int_0^1 \left\{ \xi_{p1} f_j^e(\xi_l - 2\xi_{p1}\xi) \right. \\ \left. + \xi_{p2} f_j^e(\xi_l + 2\xi_{p2}\xi) \right\} \ln\left(\frac{1}{\xi}\right) d\xi \quad (21)$$

where ξ_l is the location of the singularity in the reference element, $\xi_{p1} = (1 + \xi_l)/2$ and $\xi_{p2} = (1 - \xi_l)/2$. The first integral in eqn (21) is regular and can be evaluated with Gauss integration; the second integral is evaluated with

Berthod–Zabrowsky's method, which provides similar accuracy as the Gauss integration for logarithmically singular kernels.

For the singular radiation integrals $K_{r,l}^i$, the procedure is identical to that for $I_{d_{ij}}^e$, and eqn (21) is applicable, with $f_j^e = \sin(k_m^i z(\xi))(\partial s^e(\xi)/\partial \xi)$.

In the Neuman integrals (eqn (15)), when $j = l$, we similarly have $\lim_{kr \rightarrow 0} H_1^{(1)}(kr) = 2j/(\pi kr)$.⁷ Hence, the kernel behaves as the kernel for potential flow theory and these integrals are not singular. For small r , however, they have a strongly varying kernel and the accuracy of their Gauss integration can be improved, following Grilli *et al.*,⁸ by first performing an integration by parts; in doing so, the resulting integrals have a more gently varying kernel and can be more accurately evaluated using Gauss integration. We thus have,⁸ for the Neuman integral for the e th element,

$$I_{n_{ij}}^e = - \int_{-1}^{+1} f_j^e(\xi) \frac{\partial r}{\partial n} \left\{ k \frac{j}{4} H_1^{(1)}(kr) - \frac{1}{2\pi r} \right\} d\xi \\ - \frac{1}{2\pi} \int_{-1}^{+1} f_j^e(\xi) \frac{1}{r} \frac{\partial r}{\partial n} d\xi \quad (22)$$

with $\partial r/\partial n = (\mathbf{r} \cdot \mathbf{n})/r$. The first integral in eqn (22) is evaluated with Gauss integration and the second integral is transformed as

$$- \frac{1}{2\pi} \int_{-1}^{+1} f_j^e(\xi) \frac{1}{r} \frac{\partial r}{\partial n} d\xi \\ = \pm \frac{1}{2\pi} \left\{ \delta_{j1} \arctan(v(-1)) - \delta_{j(d+1)} \arctan(v(1)) \right\} \\ - \frac{1}{2\pi} \int_{-1}^{+1} \frac{dN_j^d(\xi)}{d\xi} \arctan(v(\xi)) d\xi \quad (23)$$

where 1 and $d + 1$ denote local indices of the first and last nodes of element e , respectively, and the right-hand-side integral is evaluated with Gauss integration, and

$$v(\xi) = \frac{z(\xi) - z_l}{x(\xi) - x_l} \quad \text{or} \quad \frac{x(\xi) - x_l}{z(\xi) - z_l} \quad (24)$$

depending on the element main orientation,⁸ with the plus or minus sign selected in eqn (23), respectively.

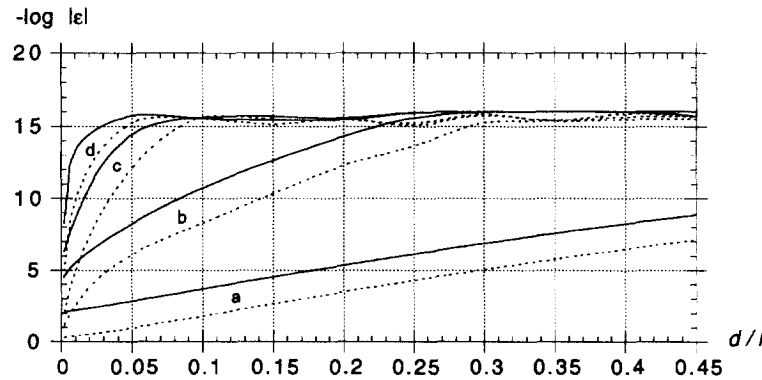


Fig. 2. Maximum integration error ϵ for adaptive integration versus relative distance d/l , for an exterior collocation node at distance d from a quadratic element of length l . Binary subdivisions $s =$ (a) 0; (b) 2; (c) 4; (d) 6. (—) Dirichlet integrals, $I_{d_{ij}}^e$; (---) Neuman integrals, $I_{n_{ij}}^e$.

2.6 Quasi-singular integration

Domain geometries in shallow water typically have aspect ratios d/l much less than one, where d is the water depth and l is the range. In fact, the aspect ratio in all of the applications in Section 4 is less than $1/30$, and problems with geometries having larger ranges are of even greater practical interest.

Geometries with small aspect ratios lead to situations where BEM discretization nodes and elements of the surface and bottom boundaries are relatively close to one another, such that the distance from the node on one side may be significantly less than the element length on the opposite side. Such close proximity causes inaccuracies for the Gauss integration of both types of (regular) BIE integrals (eqns (14) and (15)), using a fixed number of Gauss points, due to their strongly varying kernel as the distance r approaches zero. The proximity of nodes at the apex of wedge-type geometries (Fig. 1(b)) and at other corners also causes similar errors.

More specifically, as the distance r between an external node and the integrated element decreases, the order of variation of the integral kernels increases (in the sense of a Taylor series expansion for small r). In order to account for this, the number of Gauss integration points per element should be increased. As regular BEM integrals are usually performed using a fixed number of Gauss points, N_p , improved accuracy may be achieved through using the *adaptive integration* technique implemented by Grilli and Svendsen³ and Grilli and Subramanya¹⁰ for Laplace's equation, in which the number of integration points is increased through a binary subdivision of the reference element. Thus, when the distance between a collocation node and the integration points becomes small relative to the element length, the total number of integration points, I_p , for a given element is calculated as

$$I_p = 2^s N_p \quad (25)$$

where s denotes the number of binary subdivisions of the element.

Following Grilli and Subramanya,¹⁰ the accuracy of this adaptive integration technique was assessed for the present problem by calculating both types of integrals, for a single straight quadratic element, as a function of the ratio d/l of the external node distance to the element length, for various numbers of binary subdivisions, using $N_p = 10$ (Fig. 2). This was done, first, for a very accurate case, using ten binary subdivisions, $s = 10$, i.e. $I_p = 10\,240$ actual integration points. The same element was then integrated using fewer numbers of binary subdivisions, $s = 0, 2, 4$ and 6 , and errors ϵ with respect to the case with $s = 10$ were calculated.

As Fig. 2 indicates, for a given s , a decrease in d/l leads to a loss of accuracy of the integrals that may reach several orders of magnitude. Based on these results, in the BEM model, the criteria summarized in Table 1 is used in order to achieve a maximum error of $|\epsilon| \approx 10^{-16}$ in the integrals—the double-precision machine accuracy.

Table 1. Binary subdivisions s used in the adaptive integrations of regular integrals, for ranges of ratios of distance d of an external node to a BEM element of length l

$(d/l)^{\min}$	$(d/l)^{\max}$	s
	>1.0	0
1.0	0.3	2
0.3	0.1	4
0.1	0.05	6
<0.05		8

2.7 Corner solution

Particular attention is required to represent the solution and boundary conditions at corners of the computational domain. These are defined as points of geometric and/or boundary condition discontinuity. In the HBEM model, corners are represented by 'double-nodes', which are two nodes at the same location corresponding to two adjoining sides.⁵ The two nodes thus have different outward normal vectors and different normal potential gradients; yet the potential must be continuous and, therefore, both corner nodes must have the same value for the potential, whether specified through boundary conditions or found as a solution of the problem.

The typical shallow water problems, such as sketched in Fig. 1, have two types of intersecting boundaries for which: (i) one node has a known potential and the other has a known normal gradient (e.g. free surface and lateral sides); (ii) only the normal gradient is known for each node (e.g. bottom and lateral sides). The remaining parts of the boundary are assumed to have a continuous tangent. Case (i) is handled by substituting the known potential in the system of equations, for both nodes of a corner. Case (ii) is handled by modifying the system of equations so that the unknown potentials at the double node are equal after solution.

Modifications of the algebraic system (eqn (17)), of matrix \mathbf{K} , are performed as follows. For both cases (i) and (ii), the largest matrix element on the diagonal, K^{\max} , is first determined; K^{\max} will be used as a weight factor to ensure good conditioning of the modified system. Next, the elements in the matrix row l , associated with double nodes j and l , are set to zero; this is similarly done for the l th position in the system load vector, \mathbf{P} . For case (i), where the potential, $\bar{\phi}_j$ is known at node j , the entry of the associated double node is set to, $K_{ll} = K^{\max}$, and $P_l = K^{\max} \bar{\phi}_j$. This ensures that the potentials at corner nodes j and l are equal to $\bar{\phi}_j$, after solving the system. For case (ii), the (different) normal gradients of the potential are the known field values at the double nodes. Forcing the unknown potentials at the corner nodes j and l to be equal after solving the system requires to set, $K_{ll} = K^{\max}$ and $K_{jl} = -K^{\max}$, with $P_l = 0$.

Note that these substitutions are done for the complex matrix system and special attention is required when parsing the system into the $[2N_n \times 2N_n]$ real system.

3 MODEL VALIDATION

3.1 Numerical study

The HBEM model is validated for simple geometries for which analytic solutions are known. The first test case, sketched in Fig. 3, has a rectangular domain and will be used to study: (i) the influence of the number of nodes per wavelength on the accuracy of the BEM solution; (ii) the effect of the adaptive integration technique for small domain aspect ratios; and (iii) the influence of the number of modes used in radiated fields, on the accuracy of the HBEM solution. Problems with a bottom step and a sloped geometry, more representative of shallow water propagation, will be considered next (Fig. 9); both cases have known analytic solutions. The step provides a geometry for which there is radiation on both lateral boundaries, like in Fig. 1(a), and the sloped geometry is representative of near-shore environments, such as a plane sloping beach, with only one radiation boundary on the offshore side, as in Fig. 1(b).

Note that, with a BEM method, besides the boundary discretization, no additional approximation is made to explicitly calculate the solution for the interior of the computational domain, based on the boundary solution. This is because integral equations such as eqn (13) are exact relationships (with, in this case, $\alpha = 1$). In fact, in such problems, the interior solution is usually found to be more accurate than the boundary solution. Hence, to compare results of the HBEM model to analytic solutions, only the boundary values will be used. Another important aspect is the effect of local, larger than average, boundary errors on the interior solution, as for instance occurs near and at re-entrant corner nodes on the boundary. In the BEM, since all the boundary values are used to calculate the interior solution and Green's functions decaying with the distance are used as weights in this calculation, such local errors have little influence on the interior solution, outside of a small area located around these nodes. (This was well verified in the particular computations in this paper.)

In light of these observations, to avoid giving unrealistic weight to maximum errors in the assessment of model accuracy, the error of the numerical solution for various test cases is measured by calculating the root mean square error (RMS) between the HBEM and the analytic solutions, for the N_n nodes along the boundary. The RMS error is defined as,

$$\text{RMS}(\epsilon) = \frac{1}{\phi^{\max}} \sqrt{\frac{1}{N_n} \sum_{i=1}^{N_n} (\phi_{bi} - \phi_{ai})^2} \quad (26)$$

where index b refers to the numerical solution with the HBEM model and index a to the analytical solution, and the potentials have been normalized by the maximum potential, ϕ^{\max} , calculated on the boundary. The RMS error thus provides a measure of the overall accuracy of the solution, while somewhat reducing the importance of

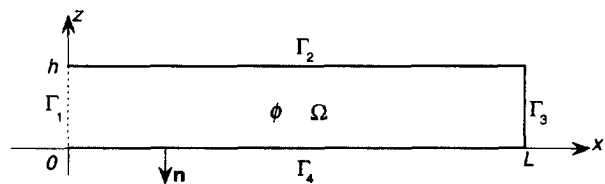


Fig. 3. Geometry and boundary conditions for rectangular domain.

large local errors. For instance, assuming there is one node in the discretization, e.g. a corner, with maximum relative error, say ϵ_c , c times larger than the average relative error for the other nodes, one can show that

$$\text{RMS}(\epsilon) \approx \epsilon_c \left(\frac{1}{c} + \frac{c}{2N_n} \right) \quad (27)$$

If $c = 3$, as will be found for the re-entrant corner in the step problem (Fig. 9), we get $\text{RMS} = 0.35$ and $0.34\epsilon_c$ for $N_n = 100$ and 200 , respectively. Thus, in this case, since N_n is much larger than c , the RMS error is about one third (i.e. $1/c$) the relative maximum nodal error.

The nodal discretization is selected by determining the number of nodes required to obtain a given minimum number of nodes n per wavelength, $\lambda = 2\pi/k$. The resulting number of nodes for a particular side in the domain is then adjusted so that an integer number of quadratic, three-node isoparametric elements ($d = 2$) can be used on the side. This technique allows for a constant element length on a given side, with a specified number of nodes per wavelength, n/λ . Ten integration points per element are used ($N_p = 10$) and adaptive integration, when performed, is done according to the criteria in Table 1.

3.2 Rectangular domain

The first and most straightforward test problem is given by specifying three rigid boundaries Γ_2 , Γ_3 , and Γ_4 , and a uniform potential on the fourth boundary Γ_1 , in the rectangular domain sketched in Fig. 3. The specified potential has a value such as to easily derive an analytic solution using separation of variables. Boundary conditions thus read,

$$\begin{aligned} \bar{\phi}(0, z) &= \frac{1}{\omega\rho_o} \cot(kL) \quad \{x=0; 0 \leq z \leq h\} \\ \frac{\partial \bar{\phi}}{\partial n} &= 0 \quad \left\{ \begin{array}{l} z=h; 0 \leq x \leq L \\ x=L; 0 \leq z \leq h \\ z=0; 0 \leq x \leq L \end{array} \right\} \end{aligned} \quad (28)$$

where h is the domain height and L is the domain length. The closed form solution to this problem is expressed as

$$\phi(x, z) = \frac{1}{\omega\rho_o} \left\{ \sin(kx) + \frac{\cos(kx)}{\tan(kL)} \right\} \quad (29)$$

As expected from the boundary conditions, there is no z variation in the solution and a typical (standing) potential

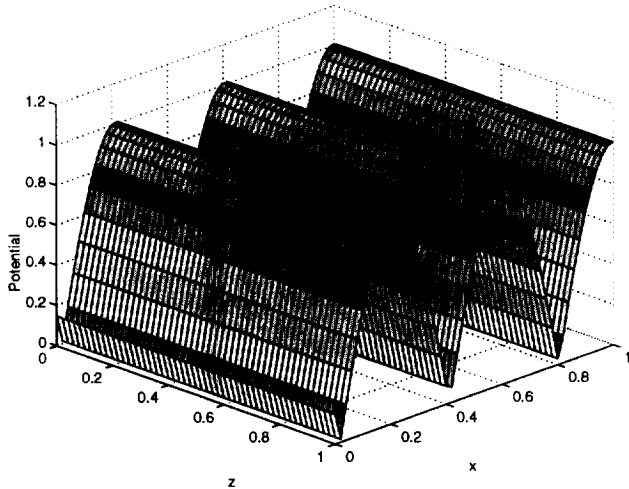


Fig. 4. Typical plot of potential over rectangular domain of Fig. 3. Wavenumber, $kh = 8$, and dimensions $h = 1, L = 1$ were used.

distribution in the domain can be calculated with eqn (29), as indicated in Fig. 4.

The exact solution (eqn (29)) is now compared with the BEM solution over a range of normalized wavenumbers kh . The test case has dimensions, $L = 1$ and $h = 1$, with $n/\lambda = 15$. The results are presented in Fig. 5. The wavenumbers for

which the solution gives the least accuracy coincide with resonance and anti-resonance modes or occur when the normal gradient and the potential equal zero at boundary Γ_1 , respectively. Resonance and anti-resonance occur according to the following relationships:

$$kh = \frac{i\pi h}{L} \text{ and } \frac{(i + \frac{1}{2})\pi h}{L} \tag{30}$$

respectively, where i is an integer value. One can see on the figure that peaks of error approximately correspond to $i = 2$ in these equations, i.e. $kh = 2\pi$ and 2.5π , respectively. It is interesting to note that the larger error at $kh = 6.5$ is not associated with resonance or anti-resonance.

Despite local inaccuracies, there is good overall agreement in Fig. 5 between analytical and numerical results, for the selected discretization, with the larger errors being less than 5% at the resonance, and less than 1% outside the resonance, frequencies. Note that errors for the normal gradient are always larger than errors for the potential.

These errors can be further reduced by refining the discretization. This is discussed in the next section.

3.2.1 Nodes per wavelength

The same rectangular geometry as in Fig. 3 is now used to demonstrate that the numerical model converges to the analytic solution as the number of nodes per wavelength is

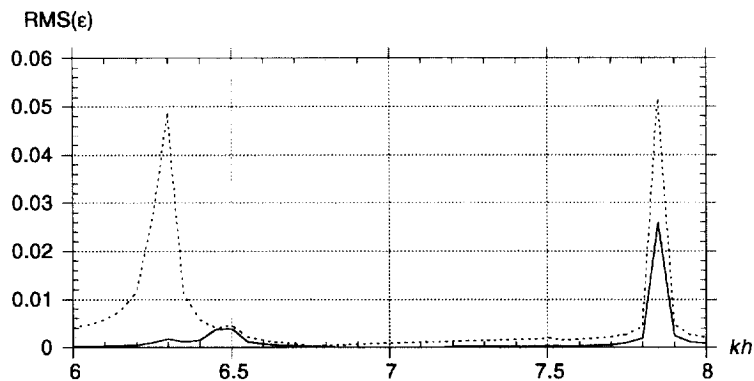


Fig. 5. RMS error for rectangular domain of Fig. 3, with $L = 1$ and $h = 1$: (—) potential; (---) normal gradient.

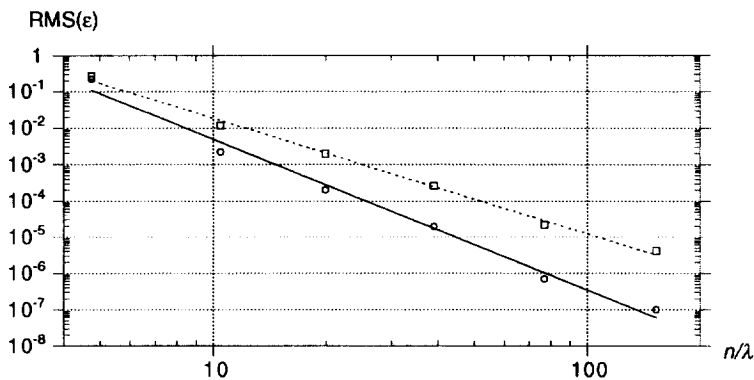


Fig. 6. Convergence of RMS error for rectangular domain of Fig. 3, with $L = 1$ and $h = 1$ and number of nodes per wavelength n/λ , for $kh = 6.6$: (— ° —) potential; (--- □ ---) normal gradient. Lines denote least-squares fits with slopes $B = -4.15$ and -3.17 , respectively.

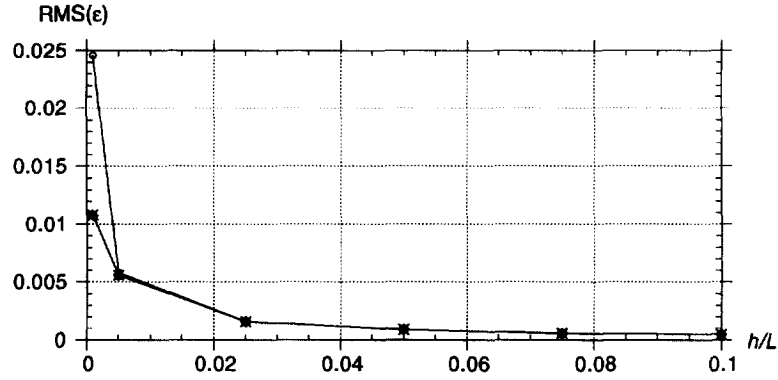


Fig. 7. RMS error for rectangular domain of Fig. 3 versus domain aspect ratio h/L with $kh = 3.5$, for binary subdivisions of non-singular integrals with $s = 0$ (\circ), 2 (\square), 4 (\diamond), 6 (\times). Calculations use 15 nodes per wavelength.

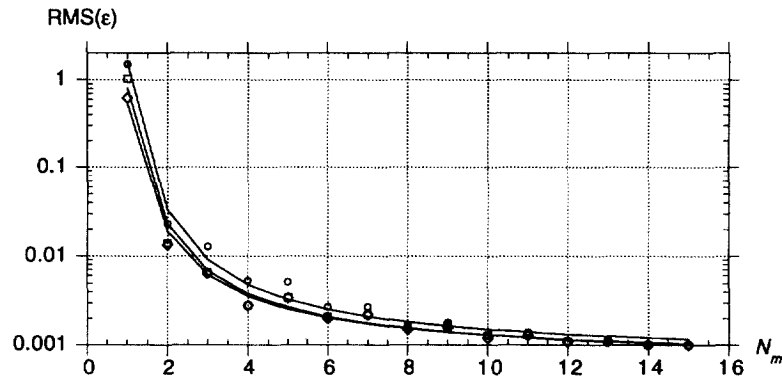


Fig. 8. Convergence of RMS error with the number of nodes N_m in radiation condition, for rectangular domain of Fig. 3, with $kh = 5$, as a function of the source location $x/h = :$ (\circ) 0.1, (\square) 0.5, (\diamond) 1.0.

increased. Fig. 6 indicates RMS errors for $kh = 6.6$, as a function of the number of nodes n per wavelength λ . Clearly, the solution converges as the number of nodes is increased. Rates of convergence can be estimated by assuming

$$\text{RMS}(\epsilon) = A \left(\frac{n}{\lambda} \right)^B \quad (31)$$

and calculating least-squares fits of the results in Fig. 6. We thus obtain $B = -4.15$ and -3.17 for the potential and its normal gradient, respectively, i.e. high convergence rates.

As noted by Jensen *et al.*,² we see in the figure that adequate resolution can be achieved with 10 nodes per wavelength. Here, however, in order to achieve better accuracy, most of the cases studied used at least 15 nodes per wavelength; 20 nodes per wavelength were used in some cases when greater accuracy was sought. The trade-off for the improved accuracy is the increased computational time required to assemble and solve the system of equations. Results show that the computational time increases with the square of the number of nodes.

3.2.2 Adaptive integration

As previously indicated, small domain aspect ratios lead to nodes and integration points (on the surface and bottom) to

be relatively close to one another and thus to inaccuracies in the regular numerical integrations. These are the so-called ‘quasi-singular’ integrals and this issue is handled using an adaptive integration technique, as illustrated in Fig. 2.

In actual wave propagation problems, however, we are usually interested in propagating waves or modes, with $kh = 2\pi h/\lambda \geq \pi/2$, corresponding to the first cut-off frequency. In addition, to ensure sufficient resolution in the BEM solution, we require a number of nodes per wavelength, $n/\lambda \geq 15$ or $\lambda/\Delta x \geq 14$, where $\Delta x = \lambda/(n-1)$ denotes the interval between two nodes on the boundary. Hence, combining these requirements, we obtain, for the relative distance $d = h$ of, say, a bottom node to a quadratic surface element of length $l = 2\Delta x$, $d/l \geq 1.75$. Therefore, according to this criterion, our computational problems are always out of the range for which adaptive integration is really required (Table 1) and, in most cases, little benefit should be expected in using it.

This is illustrated in Fig. 7, which shows RMS errors for the potential and its normal gradient, as the domain aspect ratio h/L decreases, for the rectangular domain of Fig. 3, using $kh = 3.5$ and $n/\lambda = 15$. In most of the cases reported on the figure, no significant improvement in accuracy is observed by increasing the number s of binary subdivisions. A slight gradual increase in error is observed as h/L

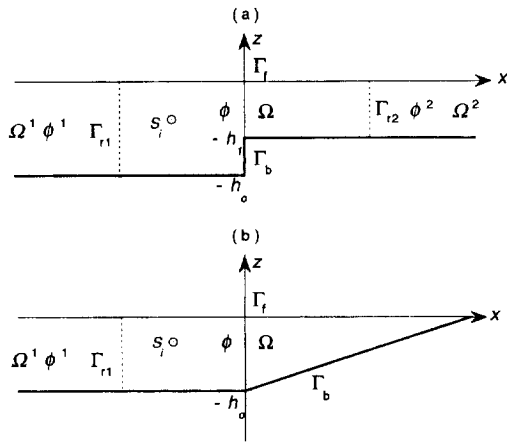


Fig. 9. Sketches of computational domain for: (a) bottom step; (b) sloping bottom.

decreases but, as discussed in Refs. ^{10,3}, this increase can be attributed to the increase in the discretized system matrix condition number and the resulting loss of accuracy of the solution, due to truncation and round-off errors. For very small $h/L \leq 0.005$, the latter errors become larger and some reduction in errors can be achieved by improving the accuracy of the integrations, i.e. using $s = 2$ binary subdivisions; no further reduction is obtained, however, for larger numbers of subdivisions.

3.2.3 Number of modes in radiated fields

The influence of the number of modes N_m , used to represent radiated fields, on the accuracy of the solution is determined for the simple rectangular domain of Fig. 3. Here, the four boundaries are specified as in Fig. 1(b): a radiation condition on Γ_1 ; a pressure release on Γ_2 ; and no-flow conditions on

lateral and bottom boundaries Γ_3 and Γ_4 . The excitation is provided by a point source located at (x_s, z_s) .

The boundary discretization and non-dimensional wave-number were kept constant while the number of modes N_m was increased in the radiation condition (eqn (11)). Computations were done for three normalized distances of the source, $x_s/h = 0.1, 0.5, 1.0$, to the radiation boundary Γ_1 , with $z_s = h/2$. The influence of N_m on the error for the potential is shown in Fig. 8. The non-dimensional wave-number is $kh = 5$, which corresponds to two propagating modes. The convergence rapidly levels up as soon as the number of computational modes exceeds the number of propagating modes.

The plot also indicates that an increased proximity between the source and the lateral radiation boundary requires using more computational modes on the radiation boundary to achieve the same accuracy. The convergence appears to become independent of the source location when the source is at least $x_s = 0.5h$ from the boundary; for smaller distances, more modes are required. The same behavior is noted for other cases having various numbers of propagating modes. This indicates that just a few more computational modes than propagating modes are necessary for accurately specifying the radiation condition. In practice, as the number of modes has little influence on the computational time, several more modes are often used.

3.3 Bottom step and sloping geometry

The step-up geometry is presented in Fig. 9(a). An analytic solution for this problem was developed by Stepanishen *et al.*,⁴ based on matched eigenfunction expansions; it is used here to validate the HBEM model.

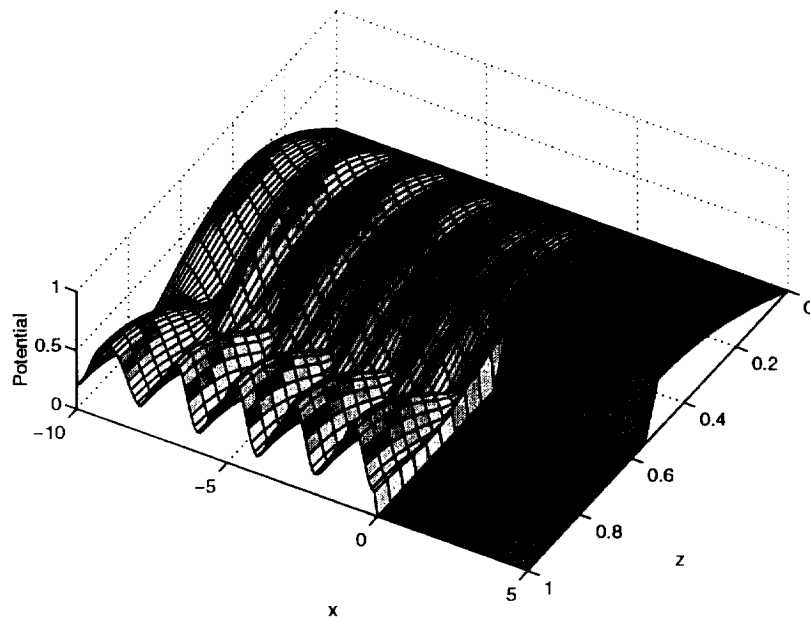


Fig. 10. Typical plot of potential for the step geometry of Fig. 9(a), with $h_1/h_0 = 0.5$ and $kh_0 = 5$ (analytic solution). The source is located at $x_s = -8$ and $z_s = -0.5$ and 10 modes are used in the radiation conditions.

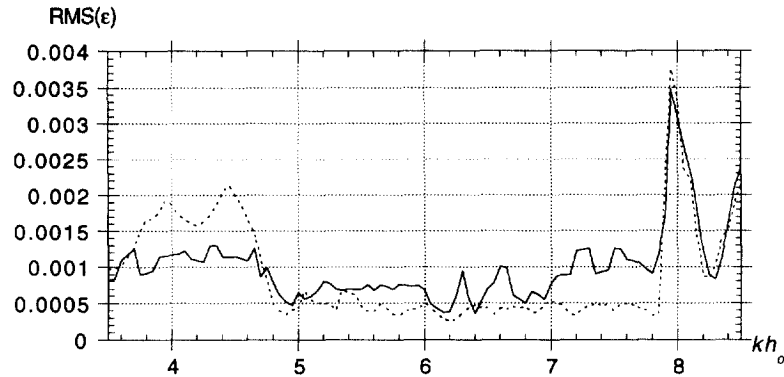


Fig. 11. RMS error of the step geometry of Fig. 9(a) with $h_1/h_0 = 0.5$, for: (—) potential; and (---) normal gradient; 15 computational modes and 20 nodes per wavelength were used.

Both solutions are calculated for a step depth ratio of $h_1/h_0 = 0.5$, with an excitation source of strength $S = 1$ located at $x_s = -8$ and $z_s = -0.5$, over a range of non-dimensional wavenumbers kh_0 which incorporates one to four propagating modes in the deeper water region and one to two propagating modes in the shallower region. As an example, Fig. 10 shows the potential field obtained for $kh_0 = 5$ using the analytic solution (in this case, however, due to the very small errors, no noticeable difference would be observed for the HBEM internal solution); there are two propagating modes in the region Ω^1 and one propagating mode in region Ω^2 over the step.

In the BEM results, the corners resulting from the step discontinuity on the bottom are the greatest source of error. Corner nodes indeed represent locations with two normal directions where acoustic waves undertake large diffraction, i.e. large local variations. In order to reduce these inaccuracies, the step corners were rounded with a radius, $R = \lambda/100$;

no significant influence of this slight change in geometry was observed outside of the corner regions. Despite significant improvements of the corner solution, however, the largest errors still occurred at the step corner nodes, and were observed to be maximum for the re-entrant corner node (about $c = 3$ times the average error of the other nodes). This is due to the larger variations still existing for the solution over corner elements, which the limited discretization cannot accurately model. Fig. 11 shows errors for the potential and its normal gradient as compared to the analytic solution; despite larger local errors at the step corners, the maximum RMS errors are less than 0.37%.

The sloping geometry of Fig. 9(b) provides an approximate description of a coastal environment with a mildly sloping bottom, which may be thought of as a beach. A so-called 'pie' approximate analytic solution was developed by Stepanishen *et al.*,⁴ based on matched eigenfunction expansions in polar coordinates. This solution is applicable

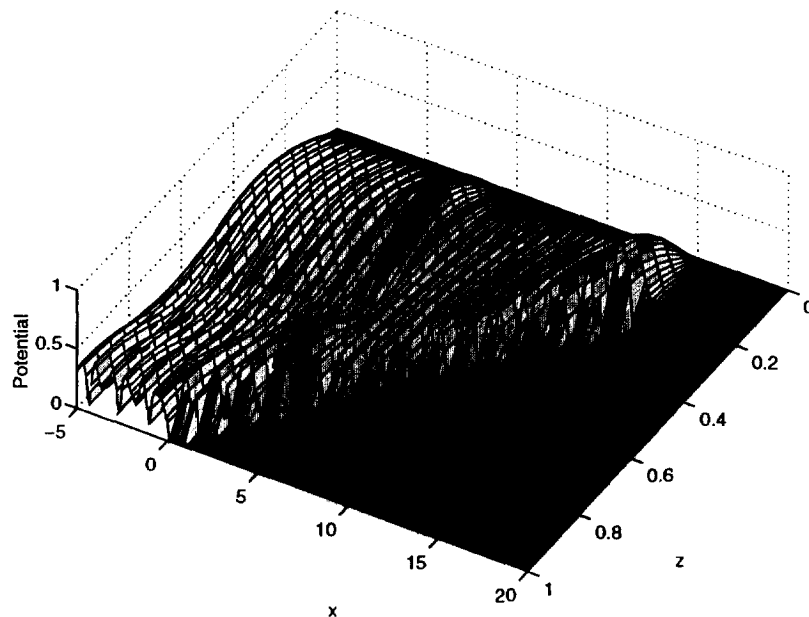


Fig. 12. Typical plot of potential for the sloping geometry of Fig. 9(b), with a slope 1:20 and $kh_0 = 6$ (analytic 'pie' solution). The source is located at $x_s = -8$ and $z_s = -0.5$ and five modes are used in the radiation conditions.

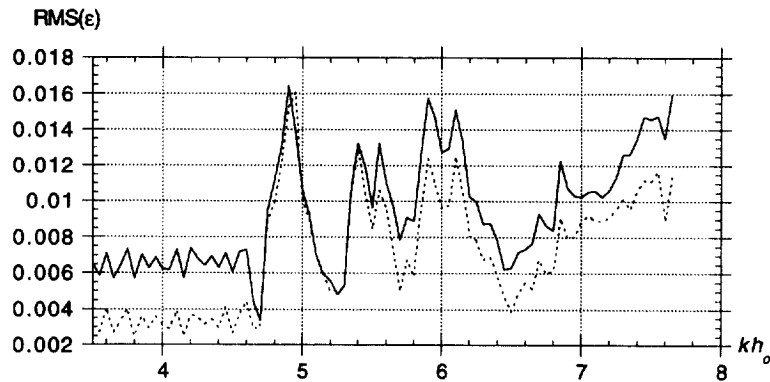


Fig. 13. RMS error of the sloping geometry of Fig. 9(b), with slope 1:20, for: (—) potential; and (---) normal gradient; 15 computational modes and 20 nodes per wavelength were used.

for mildly sloping geometries and is used here to validate the HBEM model for a 1:20 slope. As an example, Fig. 12 shows the potential field obtained for $kh_o = 6$ using the analytic solution (in this case, as indicated before, the HBEM internal solution would likely be even more accurate); there are two propagating modes in region Ω^1 and then, over the slope, these modes are being successively turned off as depth reduces; eventually, for very small depth, only evanescent modes can be seen.

Fig. 13 shows errors for the potential and its normal gradient as compared to the analytic solution; due to inaccuracies in the analytic solution,⁴ however, particularly at higher frequencies, errors in the HBEM model seemed to be slightly larger than for the other problems. Bearing this in mind, let us consider the plots of RMS errors, and we see that the HBEM solution compares favorably with the pie solution, in between larger peaks of error, which can be attributed to spurious behavior of the analytic solution.

4 APPLICATIONS

The validated HBEM model can now be used for solving problems with more irregular boundary geometries. There exists a variety of shallow water problems that are of interest. However, recent shallow water acoustic field experiments by Badiy et al.¹¹ indicated that interesting transmission phenomena can occur over ‘bumps’ in the bottom. In particular, they found that the transmission of

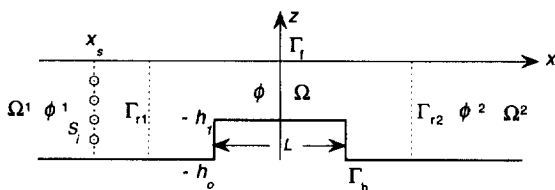


Fig. 14. Geometry for rectangular obstacle on the bottom with height $(h_o - h_1)$, and length L , defined by three regions of depths h_o , h_1 , and h_o .

low frequency acoustic energy seems to be most affected by the presence of a bump (i.e. reduced), and is also a function of the azimuthal direction (i.e. of the width of the bump).

In an attempt to qualitatively explain some of the findings of Badiy et al.,¹¹ we concentrated here on a problem in which acoustic waves generated by sources propagate over a ‘bump’ on the bottom (Fig. 1(a)). To both further simplify this problem and allow comparisons, at a later stage, with semi-analytical solutions such as in Ref. ⁴, we selected an idealized rectangular ‘bump’ geometry defined by three separate regions (Fig. 14). The first, deeper water region Ω^1 , with depth h_o , is the one containing the source(s) and radiation of waves towards $x \rightarrow -\infty$; the second shallower region Ω represents the region containing the rectangular bump of height $(h_o - h_1)$ and length L , which has a greater cut-off frequency than the deeper regions; and the third region Ω^2 , here with the same depth h_o as in the first region, provides radiation for $x \rightarrow \infty$.

As discussed in Section 1, the expectation for the acoustic propagation in this problem is that, at low frequencies, a phenomenon similar to ‘tunneling’ occurs. For the bump geometry, we thus anticipate that there will be leakage of energy across the shallower depth from region Ω^1 to Ω^2 . Over the bump in the middle region, there will thus be purely evanescent waves for frequencies just below the first cut-off frequency, yet regions Ω^1 and Ω^2 will have higher cut-off frequencies, accommodating propagating modes. Since the amplitude of the evanescent waves decreases exponentially with distance, the length L of the bump will influence the amount of energy transmitted into region Ω^2 .

As a last simplification before solving this problem, we will assume that only the first mode is propagated. This can be achieved by specifying a vertical line source at $x = x_s$, using N_s point sources at the center of segments of equal length, $\Delta z_{s_i} = h_o/N_s$, with strengths S_i calculated as (Fig. 14)

$$S_i = 2\Delta z_{s_i} \sin(k_1^1 z_{s_i}) \quad (32)$$

where k_1^1 denotes the wavenumber for the first mode in

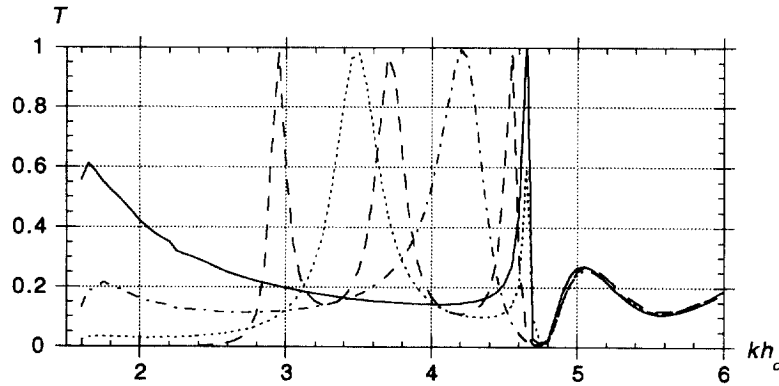


Fig. 15. Transmission coefficient T for the first acoustic mode over a rectangular obstacle, versus kh_0 , for depth ratio, $h_1/h_0 = 0.6$. The non-dimensional step length, $L/h_1 =$: (—) 0.2, (---) 0.5, (- - -) 1.0, (· · ·) 2.0. The wavenumber that the first mode turns on over the bump is $kh_0 = 2.65$.

region Ω^1 . Hence, using eqn (7), we obtain

$$S_i = 2 \frac{h_0}{N_s} \sin\left(\frac{\pi z_{s_i}}{2h_0}\right) \quad (33)$$

As done previously, to avoid sharp discontinuities and inaccuracies in the BEM results, the corners of the rectangular bump are slightly rounded with a normalized radius of curvature of $R/h_0 = 0.02$. The curvature of the corners is resolved by simply increasing the density of nodes.

The amount of energy transmitted into region Ω^2 can be represented in terms of the power transmission coefficient,

$$T = \frac{W_T}{W_1} \quad (34)$$

where W_T is the transmitted power at the right lateral boundary Γ_{r2} , and W_1 is the incident power from the vertical line of sources at $x = x_s$. The acoustic power propagating through a vertical line at x can be calculated as

$$W(x) = \frac{1}{2} \Re \left\{ \int_{-h_0}^0 p(x, z) u^*(x, z) dz \right\} \quad (35)$$

where p is the complex pressure, u is the complex velocity in the x direction, and the star denotes the complex conjugate. The transmitted power is determined by evaluating eqn (35) over Γ_{r2} , using the potential and its normal gradient from the solution in the HBEM model; hence, using eqn (4),

$$W_T = \frac{1}{2} \Re \left\{ j \rho_0 k c \int_{\Gamma_{r2}} \phi \frac{\partial \phi^*}{\partial n} d\Gamma \right\} \quad (36)$$

The resulting integral is evaluated numerically. The incident power is evaluated the same way, but the incident pressure and velocity from the excitation sources in region Ω^1 are determined as follows.⁴

$$p(x, z) = \rho_0 k c \sum_{i=1}^{N_s} \sum_{m=1}^{N_m} \frac{S_i \sin(k_m^1 z) \sin(k_m^1 z_{s_i})}{h_0 \sqrt{k^2 - k_m^{12}}} \times e^{j\sqrt{k^2 - k_m^{12}}|x - x_s|}$$

$$u(x, z) = \sum_{i=1}^{N_s} \sum_{m=1}^{N_m} \frac{S_i \sin(k_m^1 z) \sin(k_m^1 z_{s_i})}{h_0} e^{j\sqrt{k^2 - k_m^{12}}|x - x_s|} \quad (37)$$

where the position x in range may be any location in region Ω^1 , and k_m^1 denotes wavenumbers for N_m modes in region Ω^1 , calculated as in eqn (7).

The plot in Fig. 15 shows the power transmission coefficient T in region Ω^2 , for a range of frequencies and various step lengths, with a step depth $h_1/h_0 = 0.6$. The normalized bump lengths are given as $L/h_1 = 0.2, 0.5, 1.0, 2.0$. Region Ω^1 contains $N_s = 9$ sources weighted to excite the first mode, according to eqn (33). The non-dimensional wavenumber associated with the first cut-off frequency over the bump is $kh_0 = 2.65$. Below this wavenumber, the modes over the bump in the middle region Ω are purely evanescent and energy is transmitted into region Ω^2 through a ‘tunneling’ effect. This is confirmed in Fig. 15. Clearly, as the length of the bump increases, less energy is allowed to propagate at lower frequencies. This is due to the fact that the energy associated with the evanescent modes decreases exponentially with distance from its point of generation. Therefore the shorter bumps provide greater transmission.

According to the results above, given the same bump length, the bumps with greater depth should also provide greater transmission. This is confirmed in Fig. 16 where the shallower bumps with shorter lengths provide the greatest transmission of energy. The curves represent the transmission coefficient for various non-dimensional bump length, L/h_0 , as a function of the non-dimensional bump depth, h_1/h_0 , with the wavenumber, kh_0 , being constant. Greater transmission is clearly a result of the fact that the shallower the bump, the less the discontinuity between regions Ω^1 and Ω , and regions Ω and Ω^2 .

5 CONCLUSIONS

A hybrid numerical model combining a boundary element method (BEM) and eigenfunction expansions for representing

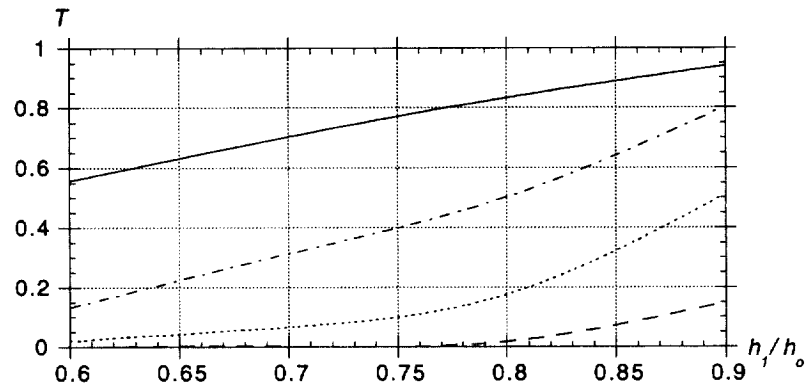


Fig. 16. Transmission coefficient T for the first acoustic mode over a rectangular obstacle, versus h_1/h_0 , for $kh_0 = 1.60$. The non-dimensional step length, $L/h_1 =$: (—) 0.2, (---) 0.5, (- - -) 1.0, (— — —) 2.0.

the radiated fields (HBEM) was developed and validated for the acoustic wave propagation in shallow water.

For harmonic waves, the governing Helmholtz equation is expressed as a boundary integral equation and solved using a higher-order BEM in which regular integrals are calculated by Gauss integration, and various kernel transformations are applied to singular integrals before integrating them with a Gauss-like method applicable to logarithmically singular kernels. Quasi-singular integrals, which occur when an external node is very close to one element, are accurately calculated using an adaptive integration technique; for computational domains with very small aspect ratios, representative of shallow water environments, this technique provides for very accurate results.

The HBEM model was validated by comparing the numerical solution to analytic solutions for problems with simple boundary geometries (e.g. rectangular, step, and sloped domains). Results indicate good agreement between the two solutions:

- (i) an increase in node resolution shows a high rate of convergence of the numerical solution; in practice, 15 nodes per wavelength are found sufficient to ensure a good accuracy of the results;
- (ii) adaptive integrations for computational domains with high aspect ratios are found to be unnecessary in most cases, due to the requirement (i) for sufficient number of nodes per wavelength in the BEM discretization; these nevertheless improve the solution in extreme cases when the discretized system conditioning starts deteriorating ($h/l < 0.005$);
- (iii) an increase in the number of modes used in radiated fields shows high convergence rate of the solution when only a few more modes than the number of propagating modes are used; and
- (iv) results for a bottom step with $h_1/h_0 = 0.5$ and a 1:20 slope, which are representative of shallow water environments, indicate good accuracy of the HBEM solution; more discussions about the physical meaning of results for these cases can be found in Stepanishen et al.;⁴ note that the so-called analytic 'pie', solution,

used as a reference for the sloping geometry, has inherent inaccuracies for specific frequencies and, hence, the HBEM solution may be more accurate than the errors indicated in such cases.

Finally, the validated HBEM model is used to study problems for which the geometry prevents or complicates an analytic approach. The transmission of energy over a bump on the bottom, in a manner similar to the 'tunneling' phenomenon, is investigated. For simplicity, an idealized rectangular geometry is selected for the bump, and only the first acoustic mode is propagated. The study indicates that:

- (i) below the first cut-off frequency over the bump, propagating modes are excited in the far right region Ω^2 by exponentially decaying (with distance) evanescent modes occurring over the bump, in region Ω ;
- (ii) this tunneling-like effect appears to be most significant for the bumps with the shortest length L and greatest depth h_1 ; this is intuitively sensible since a deep bump provides a larger vertical section for the evanescent modes to act upon and the bumps having the shortest length will have the greatest amplitude of evanescent modes at the bump extremity; and
- (iii) comparison of HBEM results for a rectangular bump and a semi-analytical solution, as well as more discussions of results can be found in Stepanishen et al.⁴

Many other cases, not reported here, were calculated for rectangular bumps of various geometries and results all showed a similar qualitative behavior; this indicates that the HBEM model can be used as a tool for investigating acoustic propagation in shallow water, for boundary geometries for which there is no analytical solution. In particular, it is believed that results of recent field experiments by Badiey et al.,¹¹ in which a similar tunneling effect was observed at low frequency, could be qualitatively reproduced in the model.

Some future studies may also involve variations with either or both the bottom and free surface, as well as a variety of domains containing different target types.

ACKNOWLEDGEMENTS

This research was supported by the US Office of Naval Research (Ocean Acoustics Division), under grant N00014-94-I-0565 from the US Department of the Navy, Office of the Chief of Naval Research. The information reported in this work does not necessarily reflect the position of the US Government.

REFERENCES

1. Urick, R. T. *Principles of Underwater Sound for Engineers*. McGraw-Hill Book Co., New York, 1967.
2. Jensen, F., Kuperman, W., Porter, M. & Schmidt, H. *Computational Ocean Acoustics*. AIP Press, New York, 1994.
3. Grilli, S. T. and Svendsen, I. A. Corner problems and global accuracy in the boundary element solution of nonlinear wave flows. *Engng. Analysis with Boundary Elements*, 1990, **7**(4), 78–195.
4. Stepanishen, P., Pedersen, T. & Grilli, S. T., An analytical method for shallow water acoustic propagation over irregular bottom. *J. Sound and Vibrations*, 1998.
5. Brebbia, C. A. *The Boundary Element Method for Engineers*. Wiley, New York, 1978.
6. Demidovitch, B. & Marion, I. *Eléments De Calcul Numérique*. Editions of Moscow, 1979.
7. Abramowitz, M. & Stegun, I. *Handbook of Mathematical Functions*. Dover Publications, Inc., New York, 1972, pp. 360–361.
8. Grilli, S. T., Skourup, J. and Svendsen, I. A. An efficient boundary element method for nonlinear water waves. *Engng. Analysis with Boundary Elements*, 1989, **6**(2), 97–107.
9. Stroud, A. H. & Secrest, D. *Gaussian Quadrature Formulas*. Prentice-Hall International Inc., London, 1966.
10. Grilli, S.T. and Subramanya, R. Quasi-singular integrals in the modeling of nonlinear water waves in shallow water. *Engng. Analysis with Boundary Elements*, 1994, **13**(2), 181–191.
11. Badiy, M., Jaya, I. and Cheng, A. H.-D. Shallow water acoustic/geoacoustic experiment at the New Jersey Atlantic generating station site. *J. Acoust Soc. Am.*, 1994, **96**(6), 3593–3604.